Available online at www.sciencedirect.com
SCIENCE DIRECT®
Journal of Computational Physics 212 (2006) 662–680
JOURNAL OF COMPUTATIONAL PHYSICS
www.elsevier.com/locate/jcp

Immersed boundary method for flow around an arbitrarily moving body

Dokyun Kim, Haecheon Choi *

School of Mechanical and Aerospace Engineering, Seoul National University, San 56-1 Shinlim-dong, Kwank-ku, Seoul 151-744, Republic of Korea

Received 15 November 2004; received in revised form 4 July 2005; accepted 18 July 2005
Available online 1 September 2005

Abstract

For the simulation of flow around an arbitrarily moving body, an immersed boundary method is developed in a non-inertial reference frame that is fixed to the body. The Navier–Stokes equation is formulated in a conservative form such that the force terms due to the rotation and the translational and rotational accelerations are included in the nonlinear term. In order to satisfy the no-slip condition on the body surface, momentum forcing and mass source/sink are applied on the body surface or inside the body. The numerical method is based on a finite volume approach on a staggered mesh together with a fractional-step method. The present numerical method is applied to both the forced motion and fluid–structure interaction problems. In the latter, we solve fully coupled Navier–Stokes and dynamic equations for the moving body without introducing any iteration. Four different flow problems are tested and the results are in excellent agreements with previous numerical and experimental ones.
© 2005 Elsevier Inc. All rights reserved.

PACS: 47.11+j

Keywords: Immersed boundary method; Arbitrarily moving body; Non-inertial reference frame; Fluid–structure interaction; Momentum forcing; Mass source or sink

1. Introduction

One of the important issues in computational fluid dynamics (CFD) is to develop a numerical method for the simulation of flow around an arbitrarily moving body. However, there are certain difficulties in

* Corresponding author. Also at: National CRI Center for Turbulence and Flow Control Research, Institute of Advanced Machinery and Design, Seoul National University, Republic of Korea. Tel.: +82 2 880 8361; fax: +82 2 878 3662.
E-mail address: choi@socrates.snu.ac.kr (H. Choi).

0021-9991/$ - see front matter © 2005 Elsevier Inc. All rights reserved.
doi:10.1016/j.jcp.2005.07.010

establishing such a numerical method because it should handle both the arbitrary movement and complex shape of the body. So far, many numerical methods including the unstructured grid method and immersed boundary method have been applied to a stationary body with complex geometry. Among them, the immersed boundary method has recently received a special attention in the CFD community because it can handle complex geometries quite easily using the Cartesian or cylindrical grids. In this method, the grids do not coincide with the body surface and thus the no-slip condition on the immersed body surface is satisfied by providing momentum forcing inside the body. However, most of the methods developed are designed for stationary bodies.

For the simulation of flow around a moving body, both the inertial and non-inertial reference frames have been used. In the former approach, the reference frame is fixed (or moving in a constant speed) in space, and the mesh is generated at each computational time step [1], or some special techniques without regenerating grids such as the volume of fluid motion [2] and level set [3] are used in order to capture the body motion appropriately. In the latter approach, the reference frame is fixed to the moving body, and the Navier–Stokes and continuity equations are transformed into those in the non-inertial reference frame [4]. The conventional transformation in the non-inertial reference frame produces source terms in the momentum equation such as the translational acceleration, Coriolis and centrifugal acceleration terms. Except the centrifugal acceleration term that may be treated as the gradient of a potential, other terms remain in explicit source terms. Accordingly, the momentum equation is not expressed in a conservative form. The disadvantages of this non-conservative form were reported in Kley [5], who indicated that the explicit treatment of the Coriolis force may lead to erroneous results in a rotating coordinate system. Beddhu et al. [6] successfully formulated the Navier–Stokes equations in a fully conservative form without the traditional source terms in the case of a rotating reference frame. Rather unfortunately, the flow problem considered in this paper was the Ekman boundary layer only and unsteady flow problems were not solved. Accordingly, this important study has not received much attention so far.

The motion of a moving body can be classified into two types depending on how its velocity is determined. The first is the forced motion of a moving body, where the translational and rotational velocities of the body are given in time. The second is such that the velocity of the body is determined by the fluid–structure interaction from the coupled dynamic equations and Navier–Stokes equations. Conventionally, the force coefficients in the dynamic equations are discretized explicitly in time in order to decouple dynamic equations from the Navier–Stokes equations [7,8]. However, this approach does not fully describe the effect of interaction between the fluid and the structure, and produces numerical instability in some cases [9]. An alternative approach is to solve Navier–Stokes and dynamic equations implicitly in time using an iterative technique at every time step [10,11], although the computational overhead increases.

In the present study, we develop a new immersed boundary method using the conservative form of the Navier–Strokes and continuity equations in the non-inertial reference frame, in order to solve the flow around an arbitrarily moving body with complex geometry. We apply our method to both forced motion and fluid–structure interaction problems. In the latter case, we solve the fully coupled equations without any iteration. The present method is applied to four different unsteady flow problems (inline oscillation of a circular cylinder, cross-flow oscillation of a circular cylinder, vortex-induced vibration of a circular cylinder, and freely falling sphere and cube under gravity).

2. Numerical method

2.1. Navier–Stokes equations in the non-inertial reference frame

In immersed boundary methods, the no-slip condition on the immersed boundary (i.e., on the body surface) is satisfied by introducing momentum forcing into the Navier–Stokes equations, because the grids do

not coincide with the body surface. In our previous paper [12], where stationary body problems were considered, we introduced momentum forcing $\boldsymbol{f}$ into the Navier–Stokes equation to satisfy the no-slip condition on the immersed boundary, and mass source/sink q into the continuity equation to satisfy the mass conservation for the numerical cell containing the immersed boundary. In the present study, we apply this immersed boundary method to moving body problems.

As shown in Fig. 1, momentum forcing $\boldsymbol{f}$ is introduced to the body surface or inside the body depending on the relative position of grids to the body surface. The forcing points are located in a staggered fashion like the velocity components defined in a staggered mesh. Mass source/sink q is introduced at the cell center like the pressure. Note that one may introduce both momentum forcing and mass source/sink into the whole solid body, in order to get more stable solutions at high Reynolds numbers (see, for example, Yun et al. [13] for flow over a stationary sphere at $Re = 10^4$). In the present study, we apply both momentum forcing and mass source/sink to the whole body for better stability. Since we consider a non-inertial reference frame fixed to the body, the grids and grid locations for momentum forcing and mass source/sink do not change in time. Therefore, the procedure of determining $\boldsymbol{f}$ and q for the moving body is essentially the same as that for the stationary body. The details about how to determine $\boldsymbol{f}$ and q are fully described in Kim et al. [12] and thus we do not repeat the procedure here. Instead, we describe numerical details associated with moving body problems in the framework of immersed boundary method in this paper.

Now, let us consider the governing equations in the non-inertial reference frame. As mentioned earlier, the conventional formulation in the non-inertial reference frame produces source terms in the momentum equation. Then, the governing equations in the non-inertial reference frame become

$$\left(\frac{\partial \boldsymbol{u}_r}{\partial t}\right)_r + \nabla \cdot (\boldsymbol{u}_r \boldsymbol{u}_r) = -\nabla p + \frac{1}{Re}\nabla^2 \boldsymbol{u}_r - \boldsymbol{\Omega} \times \boldsymbol{\Omega} \times \boldsymbol{x}_r - 2\boldsymbol{\Omega} \times \boldsymbol{u}_r - \frac{\mathrm{d}\boldsymbol{\Omega}}{\mathrm{d}t} \times \boldsymbol{x}_r - \mathbb{R}^T \frac{\mathrm{d}^2 \boldsymbol{d}_a}{\mathrm{d}t^2} + \boldsymbol{f}, \tag{1}$$

$$\nabla \cdot \boldsymbol{u}_r - q = 0, \tag{2}$$

where $\boldsymbol{x}_r$ and $\boldsymbol{u}_r$ are the orthogonal coordinates and corresponding velocity vector in the non-inertial reference frame, respectively, p is the pressure, $\boldsymbol{\Omega}$ is the angular velocity of the body about the origin of the non-inertial reference frame, $\boldsymbol{d}_a$ is the origin of the non-inertial reference frame with respect to the inertial reference frame $\boldsymbol{x}_a$, Re is the Reynolds number, $\mathbb{R}$ is the rotational matrix defined as $\boldsymbol{x}_a = \mathbb{R}\boldsymbol{x}_r + \boldsymbol{d}_a$ and $\mathbb{R}^{\mathrm{T}}$ is the transpose of $\mathbb{R}$ (see Fig. 2). The rotation by an angle θ about an arbitrary axis containing the origin and having unit length direction $\boldsymbol{n} = (n_x, n_y, n_z)$ is represented by [14]

$$\mathbb{R}(\theta) = \mathbb{I} + \mathbb{W}\sin\theta + \mathbb{W}^2(1 - \cos\theta), \tag{3}$$

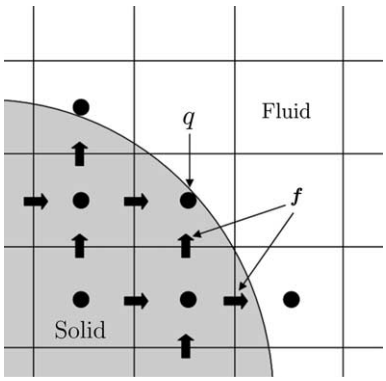

Fig. 1. Schematic diagram of the present immersed boundary method. The shaded area denotes the solid and the lines denote grid lines.

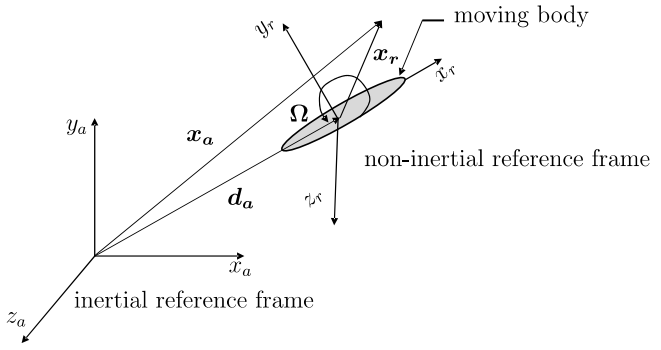

Fig. 2. Schematic diagram of the inertial and non-inertial reference frames.

where $\mathbb{I}$ is the identity matrix and

$$\mathbb{W} = \begin{bmatrix} 0 & -n_z & n_y \\ n_z & 0 & -n_x \\ -n_y & n_x & 0 \end{bmatrix}.$$

Note that $\mathbb{R}^{\mathrm{T}} = \mathbb{R}^{-1}$. The $\boldsymbol{x}_a$ and $\boldsymbol{u}_a$ are the orthogonal coordinates and corresponding velocity vector in the inertial reference frame, respectively. The relation between $\boldsymbol{u}_a$ (absolute velocity) and $\boldsymbol{u}_r$ (relative velocity) is

$$\boldsymbol{u}_a = \mathbb{R}(\boldsymbol{u}_r + \boldsymbol{\Omega} \times \boldsymbol{x}_r + \boldsymbol{u}_s), \tag{4}$$

where $\boldsymbol{u}_s = \mathbb{R}^{\mathrm{T}} \mathrm{d}\boldsymbol{d}_a/\mathrm{d}t$ is the translational velocity of the body in the non-inertial reference frame. The time derivative term in the non-inertial reference frame in Eq. (1) can be written as

$$\left(\frac{\partial \boldsymbol{u}_r}{\partial t}\right)_r = \left(\frac{\partial \boldsymbol{u}_r}{\partial t}\right)_a + (\boldsymbol{\Omega} \times \boldsymbol{x}_r + \boldsymbol{u}_s) \cdot \nabla \boldsymbol{u}_r, \tag{5}$$

where $(\,)_a$ is the time derivative in the inertial reference frame. There are four source terms in Eq. (1): $-\boldsymbol{\Omega} \times \boldsymbol{\Omega} \times \boldsymbol{x}_r$ is the centrifugal force, $-2\boldsymbol{\Omega} \times \boldsymbol{u}_r$ is the Coriolis force, and $-\mathrm{d}\boldsymbol{\Omega}/\mathrm{d}t \times \boldsymbol{x}_r$ and $-\mathbb{R}^{\mathrm{T}}\mathrm{d}^2\boldsymbol{d}_a/\mathrm{d}t^2$ are the force terms due to the rotational and translational accelerations of the body, respectively.

As developed in Beddhu et al. [6], the Navier–Stokes equations can be transformed into a conservative form in the non-inertial reference frame using Eq. (4):

$$\left(\frac{\partial \boldsymbol{u}}{\partial t}\right)_r + \nabla \cdot [(\boldsymbol{u} - \boldsymbol{v})\boldsymbol{u} + \boldsymbol{u}\boldsymbol{w}] = -\nabla p + \frac{1}{Re}\nabla^2 \boldsymbol{u} + \boldsymbol{f}, \tag{6}$$

$$\nabla \cdot \boldsymbol{u} - q = 0, \tag{7}$$

where $\boldsymbol{u} = \boldsymbol{u}_r + \boldsymbol{v} = \mathbb{R}^{\mathrm{T}}\boldsymbol{u}_a$, $\boldsymbol{v} = \boldsymbol{\Omega} \times \boldsymbol{x}_r + \boldsymbol{u}_s$ and $\boldsymbol{w} = \boldsymbol{\Omega} \times \boldsymbol{x}_r$. Thus, the source terms are now included in the nonlinear term and the governing equations become fully conservative. Note that $\boldsymbol{f}$ and q in Eqs. (6) and (7) are not the same as those in Eqs. (1) and (2). We use the same notations here for convenience. We have used this conservative formulation for all simulations because it has advantages over the non-conservative one (more discussions on this issue are given in Section 2.3).

A fractional-step method is used to solve Eqs. (6) and (7). In the fractional-step method, a pseudo-pressure is used to correct the velocity vector such that the continuity equation is satisfied at each computational time step. We use a second-order semi-implicit time advancement scheme consisting of a third-order Runge–Kutta (RK3) method for the nonlinear terms and the Crank–Nicolson method for the linear terms (the overall time accuracy is second order):

$$\frac{\hat{\boldsymbol{u}}^k - \boldsymbol{u}^{k-1}}{\Delta t} = \alpha_k L(\hat{\boldsymbol{u}}^k) + \alpha_k L(\boldsymbol{u}^{k-1}) - 2\alpha_k \nabla p^{k-1} - \gamma_k N(\boldsymbol{u}^{k-1}) - \rho_k N(\boldsymbol{u}^{k-2}) + 2\alpha_k \boldsymbol{f}^k, \tag{8}$$

$$\nabla^2 \phi^k = \frac{1}{2\alpha_k \Delta t}(\nabla \cdot \hat{\boldsymbol{u}}^k - q^k), \tag{9}$$

$$\boldsymbol{u}^k = \hat{\boldsymbol{u}}^k - 2\alpha_k \Delta t \nabla \phi^k, \tag{10}$$

$$p^k = p^{k-1} + \phi^k - \frac{\alpha_k \Delta t}{Re} \nabla^2 \phi^k, \tag{11}$$

where $L(\boldsymbol{u}) = \nabla^2 \boldsymbol{u}/Re$ and $N(\boldsymbol{u}) = \nabla \cdot [(\boldsymbol{u} - \boldsymbol{v})\boldsymbol{u} + \boldsymbol{u}\boldsymbol{w}]$. Here, $\hat{\boldsymbol{u}}$ is the intermediate velocity, ϕ is the pseudo-pressure, Δt and k are the computational time step and substep's index, respectively, and α_k, γ_k and ρ_k are the coefficients of RK3 ($\alpha_1 = 4/15$, $\gamma_1 = 8/15$, $\rho_1 = 0$; $\alpha_2 = 1/15$, $\gamma_2 = 5/12$, $\rho_2 = -17/60$; $\alpha_3 = 1/6$, $\gamma_3 = 3/4$ and $\rho_3 = -5/12$).

The second-order central difference scheme is used for all the spatial derivative terms in a staggered grid system. For example, in two dimension, $N(\boldsymbol{u}) = \nabla \cdot [(\boldsymbol{u} - \boldsymbol{v})\boldsymbol{u} + \boldsymbol{u}\boldsymbol{w}]$ is discretized as follows (see Fig. 3):

$$\begin{aligned} N_{x_r} = {} & \frac{2}{\Delta x_{r_i} + \Delta x_{r_{i-1}}} \left[\left\{ u_{x_{i+\frac{1}{2},j}} - \left(-\Omega y_{r_{j+\frac{1}{2}}} + u_{s_x} \right) \right\} u_{x_{i+\frac{1}{2},j}} - \left\{ u_{x_{i-\frac{1}{2},j}} - \left(-\Omega y_{r_{j+\frac{1}{2}}} + u_{s_x} \right) \right\} u_{x_{i-\frac{1}{2},j}} - \Omega u_{x_{i+\frac{1}{2},j}} y_{r_{j+\frac{1}{2}}} + \Omega u_{x_{i-\frac{1}{2},j}} y_{r_{j+\frac{1}{2}}} \right] \\ & + \frac{1}{\Delta y_{r_j}} \left[\left\{ u_{y_{i-\frac{1}{2},j+1}} - \left(\Omega x_{r_i} + u_{s_y} \right) \right\} u_{x_{i,j+\frac{1}{2}}} - \left\{ u_{y_{i-\frac{1}{2},j}} - \left(\Omega x_{r_i} + u_{s_y} \right) \right\} u_{x_{i,j-\frac{1}{2}}} - \Omega u_{y_{i-\frac{1}{2},j+1}} y_{r_{j+1}} + \Omega u_{y_{i-\frac{1}{2},j}} y_{r_j} \right] \end{aligned} \tag{12}$$

$$\begin{aligned} N_{y_r} = {} & \frac{1}{\Delta x_{r_i}} \left[\left\{ u_{x_{i+1,j-\frac{1}{2}}} - \left(-\Omega y_{r_j} + u_{s_x} \right) \right\} u_{y_{i+\frac{1}{2},j}} - \left\{ u_{x_{i,j-\frac{1}{2}}} - \left(-\Omega y_{r_j} + u_{s_x} \right) \right\} u_{y_{i-\frac{1}{2},j}} + \Omega u_{x_{i+1,j-\frac{1}{2}}} x_{r_{i+1}} - \Omega u_{x_{i,j-\frac{1}{2}}} x_{r_i} \right] \\ & + \frac{2}{\Delta y_{r_j} + \Delta y_{r_{j-1}}} \left[\left\{ u_{y_{i,j+\frac{1}{2}}} - (\Omega x_{r_{i+\frac{1}{2}}} + u_{s_y}) \right\} u_{y_{i,j+\frac{1}{2}}} - \left\{ u_{y_{i,j-\frac{1}{2}}} - \left(\Omega x_{r_{i+\frac{1}{2}}} + u_{s_y} \right) \right\} u_{y_{i,j-\frac{1}{2}}} + \Omega u_{y_{i,j+\frac{1}{2}}} x_{r_{i+\frac{1}{2}}} - \Omega u_{y_{i,j-\frac{1}{2}}} x_{r_{i+\frac{1}{2}}} \right]. \end{aligned} \tag{13}$$

Other terms are similarly discretized and extension to three dimension is straightforward. The system of equations discretized from Eq. (8) is solved using the approximate factorization method (see [15]). The

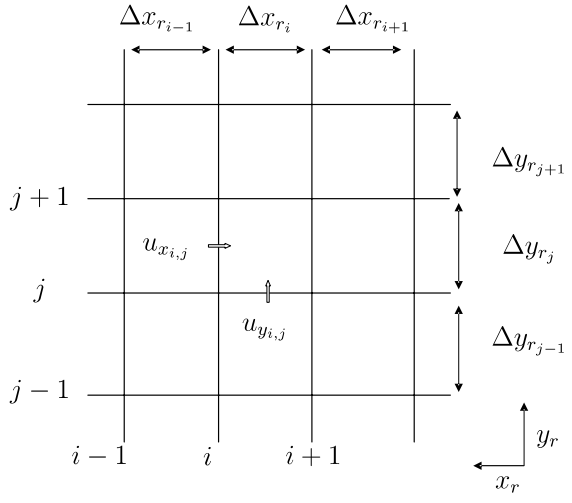

Fig. 3. Schematic diagram for spatial discretization.

equations discretized from the Poisson equation (9) by applying the second-order central difference scheme are solved using a multigrid method [16].

Momentum forcing $\boldsymbol{f}^k$ must be determined such that $\boldsymbol{u}^k$ satisfies the no-slip condition on the immersed boundary. Because $\boldsymbol{u}^k = \hat{\boldsymbol{u}}^k - 2\alpha_k \Delta t \nabla \phi^k = \hat{\boldsymbol{u}}^k + \vartheta(\Delta t^2)$, $\boldsymbol{f}^k$ is determined such that $\hat{\boldsymbol{u}}^k$ satisfies the no-slip condition instead of $\boldsymbol{u}^k$, which does not affect the overall second-order temporal accuracy as reported in Kim et al. [12]. In order to derive the momentum forcing value $\boldsymbol{f}^k$, Eq. (6) is provisionally discretized explicitly in time (e.g., RK3 for the nonlinear terms and forward Euler method for linear terms):

$$2\alpha_k \boldsymbol{f}^k = \frac{\boldsymbol{U}^k - \boldsymbol{u}^{k-1}}{\Delta t} - 2\alpha_k L(\boldsymbol{u}^{k-1}) + 2\alpha_k \nabla p^{k-1} + \gamma_k N(\boldsymbol{u}^{k-1}) + \rho_k N(\boldsymbol{u}^{k-2}), \tag{14}$$

where $\boldsymbol{U}^k$ is the velocity that we want to obtain at a forcing point by applying momentum forcing. When the forcing point coincides with the immersed boundary, $\boldsymbol{U}^k$ is equal to the velocity of the body ($\boldsymbol{v}^k = \boldsymbol{\Omega}^k \times \boldsymbol{x}_r + \boldsymbol{u}_s^k$). In general, however, the forcing point exists inside the body, and thus an interpolation procedure for the velocity $\boldsymbol{U}^k$ is required. The velocities $\tilde{\boldsymbol{u}}^k$ at grid points outside the solid but only nearby the forcing point are provisionally obtained using the same explicit scheme with $\boldsymbol{f} = 0$ as that in Eq. (14), in order to determine $\boldsymbol{U}^k$ from $\tilde{\boldsymbol{u}}^k$ and $\boldsymbol{v}^k$ using the linear or bilinear interpolation (see, for example, Fig. 4):

$$\frac{\tilde{\boldsymbol{u}}^k - \boldsymbol{u}^{k-1}}{\Delta t} = 2\alpha_k L(\boldsymbol{u}^{k-1}) - 2\alpha_k \nabla p^{k-1} - \gamma_k N(\boldsymbol{u}^{k-1}) - \rho_k N(\boldsymbol{u}^{k-2}). \tag{15}$$

The interpolation scheme for $\boldsymbol{U}^k$ and the procedure of obtaining q^k in Eq. (9) are described in detail in Kim et al. [12].

The non-dimensional force $\boldsymbol{F}_{\mathrm{N}}$ and moment $\boldsymbol{T}_{\mathrm{N}}$ exerted on a body by fluid in the non-inertial reference frame are evaluated as

$$\boldsymbol{F}_{\mathrm{N}}^k = -\left\{ \int_V \boldsymbol{f}^k \, \mathrm{d}V - V\left(\frac{\boldsymbol{u}_s^k - \boldsymbol{u}_s^{k-1}}{2\alpha_k \Delta t} + \boldsymbol{\Omega}^{k-1} \times \boldsymbol{u}_s^{k-1} \right) \right\}, \tag{16}$$

$$\boldsymbol{T}_{\mathrm{N}}^k = -\left(\int_V \boldsymbol{x}_r \times \boldsymbol{f}^k \, \mathrm{d}V - \mathbb{I}_{\mathrm{m}} \frac{\boldsymbol{\Omega}^k - \boldsymbol{\Omega}^{k-1}}{2\alpha_k \Delta t} \right), \tag{17}$$

where V and $\mathbb{I}_{\mathrm{m}}$ are the volume and moment of inertia of the body, respectively. Note that the second terms in the right-hand sides of Eqs. (16) and (17) correspond to the inertial force and moment of the body, respectively. These force and moment can be easily converted into those ($\boldsymbol{F}_{\mathrm{I}}$ and $\boldsymbol{T}_{\mathrm{I}}$) in the inertial reference frame by multiplying the rotational matrix $\mathbb{R}$:

$$\boldsymbol{F}_{\mathrm{I}}^k = \mathbb{R}^k \boldsymbol{F}_{\mathrm{N}}^k, \tag{18}$$

$$\boldsymbol{T}_{\mathrm{I}}^k = \mathbb{R}^k \boldsymbol{T}_{\mathrm{N}}^k. \tag{19}$$

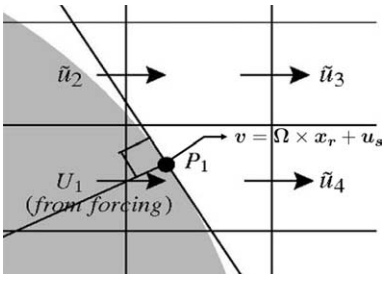

Fig. 4. Schematic diagram of the bilinear interpolation scheme.

2.2. Dynamic equations for the body motion

Three-dimensional motions of a rigid body can be described in terms of six components, $\boldsymbol{X} = (\boldsymbol{u}_s, \boldsymbol{\Omega})^{\mathrm{T}}$, where $\boldsymbol{u}_s$ and $\boldsymbol{\Omega}$ are the translational and rotational velocities of the body, respectively. When a body undergoes a forced motion, $\boldsymbol{X}$ is given. However, in the case of fluid–structure interaction, the motion of a body is not prescribed but determined by dynamic equations. The Newton's equations of the motion in the non-inertial reference frame can be written as

$$\mathbb{M}\left\{\left(\frac{\mathrm{d}\boldsymbol{u}_s}{\mathrm{d}t}\right)_r + \boldsymbol{\Omega}\times\boldsymbol{u}_s\right\} = \boldsymbol{F}_{\mathrm{N}} + \boldsymbol{F}_{\mathrm{e}}, \tag{20}$$

$$\mathbb{I}_{\mathrm{m}}\left(\frac{\mathrm{d}\boldsymbol{\Omega}}{\mathrm{d}t}\right)_r = \boldsymbol{T}_{\mathrm{N}} + \boldsymbol{T}_{\mathrm{e}}, \tag{21}$$

where $\mathbb{M}$ is the mass of the body, and $\boldsymbol{F}_{\mathrm{e}}$ and $\boldsymbol{T}_{\mathrm{e}}$ are the external force and moment on the body that are not associated with the fluid motion such as the gravitational force.

Eqs. (20) and (21) are coupled with the Navier–Stokes equations because the force $\boldsymbol{F}_{\mathrm{N}}$ and moment $\boldsymbol{T}_{\mathrm{N}}$ acting on the body are determined by the Navier–Stokes equations. In this study, $\boldsymbol{F}_{\mathrm{N}}$ and $\boldsymbol{T}_{\mathrm{N}}$ in Eqs. (20) and (21) are integrated in time using the trapezoidal method in order not to lose the full interaction effect between the fluid and structure, and $\boldsymbol{F}_{\mathrm{e}}$, $\boldsymbol{T}_{\mathrm{e}}$ and $\boldsymbol{\Omega}\times\boldsymbol{u}_s$ are done using RK3:

$$\frac{\boldsymbol{u}_s^k - \boldsymbol{u}_s^{k-1}}{\Delta t} = \alpha_k\mathbb{M}^{-1}(\boldsymbol{F}_{\mathrm{N}}^k + \boldsymbol{F}_{\mathrm{N}}^{k-1}) + \mathbb{M}^{-1}(\gamma_k\boldsymbol{F}_{\mathrm{e}}^{k-1} + \rho_k\boldsymbol{F}_{\mathrm{e}}^{k-2}) - \gamma_k\boldsymbol{\Omega}^{k-1}\times\boldsymbol{u}_s^{k-1} - \rho_k\boldsymbol{\Omega}^{k-2}\times\boldsymbol{u}_s^{k-2}, \tag{22}$$

$$\frac{\boldsymbol{\Omega}^k - \boldsymbol{\Omega}^{k-1}}{\Delta t} = \alpha_k\mathbb{I}_{\mathrm{m}}^{-1}(\boldsymbol{T}_{\mathrm{N}}^k + \boldsymbol{T}_{\mathrm{N}}^{k-1}) + \mathbb{I}_{\mathrm{m}}^{-1}(\gamma_k\boldsymbol{T}_{\mathrm{e}}^{k-1} + \rho_k\boldsymbol{T}_{\mathrm{e}}^{k-2}). \tag{23}$$

Here, $\boldsymbol{F}_{\mathrm{N}}^k$ and $\boldsymbol{T}_{\mathrm{N}}^k$ are a priori unknown and coupled with $\boldsymbol{u}_s^k$ and $\boldsymbol{\Omega}^k$ (see Eqs. (16) and (17)).

In the following, we show that one can obtain $\boldsymbol{u}_s^k$ and $\boldsymbol{\Omega}^k$ without any iterative procedure in the framework of immersed boundary method. Let us define $\boldsymbol{f}^*$ (see, for comparison, Eq. (14)) such that

$$2\alpha_k\boldsymbol{f}^* = \frac{\boldsymbol{U}^* - \boldsymbol{u}^{k-1}}{\Delta t} - 2\alpha_k L(\boldsymbol{u}^{k-1}) + 2\alpha_k\nabla p^{k-1} + \gamma_k N(\boldsymbol{u}^{k-1}) + \rho_k N(\boldsymbol{u}^{k-2}), \tag{24}$$

where $\boldsymbol{U}^*$ is the velocity at a forcing point interpolated from the body velocity at $k-1$ ($\boldsymbol{v}^{k-1} = \boldsymbol{\Omega}^{k-1}\times\boldsymbol{x}_r + \boldsymbol{u}_s^{k-1}$) and the provisional neighboring velocities $\tilde{\boldsymbol{u}}^k$ (Eq. (15)). Then, from Eqs. (14) and (24), one obtains

$$\int_V(\boldsymbol{f}^k - \boldsymbol{f}^*)\,\mathrm{d}V = \int_V\frac{\boldsymbol{U}^k - \boldsymbol{U}^*}{2\alpha_k\Delta t}\,\mathrm{d}V. \tag{25}$$

Since $\boldsymbol{U}^k$ is obtained from $\boldsymbol{v}^k$ ($=\boldsymbol{\Omega}^k\times\boldsymbol{x}_r + \boldsymbol{u}_s^k$) and the same neighboring velocities $\tilde{\boldsymbol{u}}^k$ using linear or bilinear interpolations (see Eqs. (10) and (11) in [12]), $\boldsymbol{U}^k - \boldsymbol{U}^*$ depends linearly on $\boldsymbol{u}_s^k - \boldsymbol{u}_s^{k-1}$ and $\boldsymbol{\Omega}^k - \boldsymbol{\Omega}^{k-1}$ (or $\boldsymbol{X}^k - \boldsymbol{X}^{k-1}$) and also does on the interpolation method used. Therefore, the right-hand side of Eq. (25) can be expressed as $-\mathbb{A}(\boldsymbol{X}^k - \boldsymbol{X}^{k-1})/\Delta t$, where $\mathbb{A}$ is a 3×6 matrix and its components are determined by the grid distribution. Then, the force in Eq. (16) becomes

$$\begin{aligned}\boldsymbol{F}_{\mathrm{N}}^k &= -\int_V(\boldsymbol{f}^k - \boldsymbol{f}^*)\,\mathrm{d}V - \int_V\boldsymbol{f}^*\,\mathrm{d}V + V\left(\frac{\boldsymbol{u}_s^k - \boldsymbol{u}_s^{k-1}}{2\alpha_k\Delta t} + \boldsymbol{\Omega}^{k-1}\times\boldsymbol{u}_s^{k-1}\right)\\ &= \frac{1}{\Delta t}\mathbb{A}(\boldsymbol{X}^k - \boldsymbol{X}^{k-1}) + V\frac{\boldsymbol{u}_s^k - \boldsymbol{u}_s^{k-1}}{2\alpha_k\Delta t} - \int_V\boldsymbol{f}^*\,\mathrm{d}V + V(\boldsymbol{\Omega}^{k-1}\times\boldsymbol{u}_s^{k-1})\\ &= \frac{1}{\Delta t}\mathbb{C}(\boldsymbol{X}^k - \boldsymbol{X}^{k-1}) - \int_V\boldsymbol{f}^*\,\mathrm{d}V + V(\boldsymbol{\Omega}^{k-1}\times\boldsymbol{u}_s^{k-1}),\end{aligned} \tag{26}$$

where $\mathbb{C} = \mathbb{A} + \frac{1}{2\alpha_k}[V\mathbb{I}\ \mathbf{0}]$ and $\mathbb{I}$ is the 3×3 identity matrix. Likewise, the moment in Eq. (17) can be obtained by introducing a matrix $\mathbb{B}$ that satisfies $\int_V \boldsymbol{x}_r \times (\boldsymbol{f}^k - \boldsymbol{f}^*)\,\mathrm{d}V = -\mathbb{B}(\boldsymbol{X}^k - \boldsymbol{X}^{k-1})/\Delta t$:

$$\begin{aligned}\boldsymbol{T}_{\mathrm{N}}^k &= -\int_V \boldsymbol{x}_r \times (\boldsymbol{f}^k - \boldsymbol{f}^*)\,\mathrm{d}V - \int_V \boldsymbol{x}_r \times \boldsymbol{f}^*\,\mathrm{d}V + \mathbb{I}_{\mathrm{m}}\frac{\boldsymbol{\Omega}^k - \boldsymbol{\Omega}^{k-1}}{2\alpha_k \Delta t} \\ &= \frac{1}{\Delta t}\mathbb{B}(\boldsymbol{X}^k - \boldsymbol{X}^{k-1}) + \mathbb{I}_{\mathrm{m}}\frac{\boldsymbol{\Omega}^k - \boldsymbol{\Omega}^{k-1}}{2\alpha_k \Delta t} - \int_V \boldsymbol{x}_r \times \boldsymbol{f}^*\,\mathrm{d}V = \frac{1}{\Delta t}\mathbb{D}(\boldsymbol{X}^k - \boldsymbol{X}^{k-1}) - \int_V \boldsymbol{x}_r \times \boldsymbol{f}^*\,\mathrm{d}V, \end{aligned} \tag{27}$$

where $\mathbb{B}$ and $\mathbb{D}$ ($= \mathbb{B} + \frac{1}{2\alpha_k}[\mathbf{0}\ \mathbb{I}_m]$) are 3×6 matrices and depend only on the grid distribution. Note that the matrices, $\mathbb{A}$ to $\mathbb{D}$, are calculated only once before the time marching.

Substituting Eqs. (26) and (27) into Eqs. (22) and (23), the Newton's equations become the following system of six linear equations:

$$\frac{\boldsymbol{X}^k - \boldsymbol{X}^{k-1}}{\Delta t} = \frac{1}{\Delta t}\mathbb{K}\mathbb{E}(\boldsymbol{X}^k - \boldsymbol{X}^{k-1}) + \mathbb{K}\boldsymbol{P} + \boldsymbol{Q}, \tag{28}$$

where

$$\mathbb{K} = \begin{bmatrix} \alpha_k \mathbb{M}^{-1} & \mathbf{0} \\ \mathbf{0} & \alpha_k \mathbb{I}_{\mathrm{m}}^{-1} \end{bmatrix}, \quad \mathbb{E} = \begin{bmatrix} \mathbb{C} \\ \mathbb{D} \end{bmatrix},$$

$$\boldsymbol{P} = \begin{bmatrix} -\int_V \boldsymbol{f}^*\,\mathrm{d}V + V(\boldsymbol{\Omega}^{k-1} \times \boldsymbol{u}_s^{k-1}) + \boldsymbol{F}_{\mathrm{N}}^{k-1} \\ -\int_V \boldsymbol{x}_r \times \boldsymbol{f}^*\,\mathrm{d}V + \boldsymbol{T}_{\mathrm{N}}^{k-1} \end{bmatrix},$$

$$\boldsymbol{Q} = \begin{bmatrix} \gamma_k \mathbb{M}^{-1}\boldsymbol{F}_{\mathrm{e}}^{k-1} + \rho_k \mathbb{M}^{-1}\boldsymbol{F}_{\mathrm{e}}^{k-2} - \gamma_k \boldsymbol{\Omega}^{k-1} \times \boldsymbol{u}_s^{k-1} - \rho_k \boldsymbol{\Omega}^{k-2} \times \boldsymbol{u}_s^{k-2} \\ \gamma_k \mathbb{I}_{\mathrm{m}}^{-1}\boldsymbol{T}_{\mathrm{e}}^{k-1} + \rho_k \mathbb{I}_{\mathrm{m}}^{-1}\boldsymbol{T}_{\mathrm{e}}^{k-2} \end{bmatrix}.$$

Therefore, $\boldsymbol{X}^k$ can be obtained from the following equation without any iteration:

$$\boldsymbol{X}^k = \begin{pmatrix} \boldsymbol{u}_s^k \\ \boldsymbol{\Omega}^k \end{pmatrix} = \boldsymbol{X}^{k-1} + \Delta t(\mathbb{I} - \mathbb{K}\mathbb{E})^{-1}(\mathbb{K}\boldsymbol{P} + \boldsymbol{Q}). \tag{29}$$

With $\boldsymbol{u}_s^k$ and $\boldsymbol{\Omega}^k$ (and thus $\boldsymbol{v}^k$ obtained), we solve Eqs. (8)–(11) to get $\boldsymbol{u}^k$ and p^k.

2.3. Conservative form vs. non-conservative form

As shown in Section 2.1, the Navier–stokes equations in the non-inertial reference frame can be represented in the conservative and non-conservative forms (Eqs. (1) and (6), respectively). In this section, we provide a numerical example showing that the first is superior to the latter in terms of the numerical stability. For this purpose, we consider a rotational oscillation of a circular cylinder in a static fluid that is solved, respectively, in the inertial reference frame, non-inertial reference frame with conservative form, and non-inertial reference frame with non-conservative form.

A rotational motion of a cylinder is given by a harmonic oscillation:

$$\omega_{\mathrm{c}}(t) = A_m \sin(2\pi f t), \tag{30}$$

where ω_{c} is the angular velocity of the cylinder, and A_m and f are the amplitude and frequency of the oscillation, respectively. The Reynolds number is defined as $Re = U_{\mathrm{m}}d/\nu$, where $U_{\mathrm{m}} = A_m d/2$, d is the cylinder diameter and ν is the kinematic viscosity. The computations are performed at $Re = 300$ and $f = 0.1$. In the case of inertial reference frame, the reference frame is fixed in space and the cylinder rotates with respect to the grids. On the other hand, for the non-inertial reference frame, the reference frame is fixed to the cylinder and rotates with its motion. The size of the computational domain used is $-50d < x_r < 50d$ and

$-50d < y_r < 50d$. Dirichlet boundary conditions are used for all outer boundaries as follows: for the inertial reference frame,

$$\boldsymbol{u}_a = 0; \tag{31}$$

for the non-inertial reference frame with conservative form,

$$\boldsymbol{u} = \mathbb{R}^{\mathrm{T}}\boldsymbol{u}_a = 0; \tag{32}$$

and for the non-inertial reference frame with non-conservative form (see Eq. (4)),

$$\boldsymbol{u}_r = -\boldsymbol{\Omega} \times \boldsymbol{x}_r. \tag{33}$$

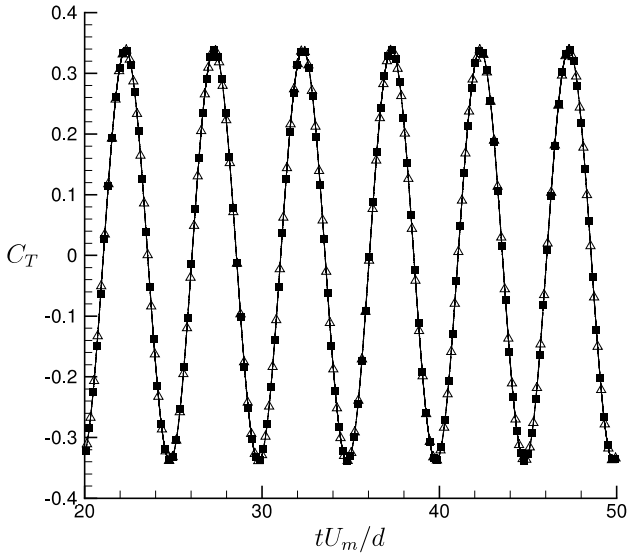

Fig. 5. Time histories of the torque coefficient for flow around a rotationally oscillating cylinder at $Re = 300$: —, inertial reference frame; ■, non-inertial reference frame with conservative form and △, non-inertial reference frame with non-conservative form.

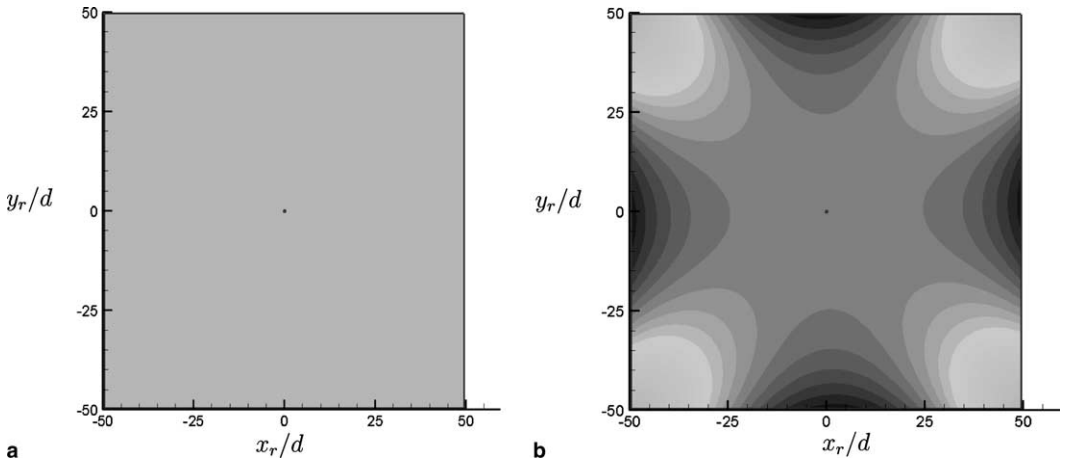

Fig. 6. Contours of the instantaneous pressure for flow around a rotationally oscillating cylinder at $Re = 300$: (a) conservative form; (b) non-conservative form. Contour levels are from −3 to 3 for (a) and from −3000 to 3000 for (b).

Note that, in the case of non-conservative form, the velocity at the outer boundary increases with increasing computational domain size.

Fig. 5 shows the time histories of the torque coefficient, $C_T = T/(0.5\rho U_m^2 d)$, obtained from three different methods, where T is the torque and ρ is the density. As is clear, the three results are identical. However, the solution eventually blows up in the case of non-conservative form due to numerical instability generated from the outer boundary condition. Fig. 6 shows the pressure contours at $tU_m/d = 100$ for the cases of conservative and non-conservative forms. A fictitious pressure field is generated from the outer boundary for the case of non-conservative form. This numerical instability is caused by the large velocity prescribed at the outer boundary, $\boldsymbol{u}_r = -\boldsymbol{\Omega} \times \boldsymbol{x}_r$. Moreover, the computational time step becomes severely restricted in the case of non-conservative form because of large $\boldsymbol{u}_r$ at the outer boundary. On the other hand, the conservative form (6) does not have such a problem because the dependent variable $\boldsymbol{u}$ is simply $\mathbb{R}^{\mathrm{T}}\boldsymbol{u}_a$ and the equation is fully conservative.

3. Numerical examples of forced motion problems

Two different unsteady flow problems are considered to show that the present numerical method accurately predicts flow induced by unsteady forced motion of a solid body. A Cartesian coordinate system in a non-inertial reference frame is applied to both test problems.

3.1. Inline oscillation of a circular cylinder

A periodic oscillation of a circular cylinder in fluid at rest is considered. There exist two non-dimensional parameters that characterize the flow induced by the motion of the cylinder. One is the Reynolds number defined as $Re = U_{\mathrm{m}}d/\nu$, where U_{m} is the maximum velocity of the cylinder during oscillation, d is the cylinder diameter, and ν is the kinematic viscosity. The other is the Keulegan–Carpenter number, $KC = U_{\mathrm{m}}/fd$, where f is the frequency of the oscillation.

The translational motion of the cylinder is given by a harmonic oscillation:

$$x_{\mathrm{c}}(t) = -A_m \sin(2\pi f t), \tag{34}$$

where x_{c} is the location of the cylinder center and A_m is the amplitude of the oscillation. Hence, the Keulegan–Carpenter number is $KC = 2\pi A_m/d$. The computation is performed at $Re = 100$ and $KC = 5$ at which the experimental and numerical results by Dütsch et al. [17] are available. The origin of the moving coordinates coincides with the center of the cylinder. The numbers of grid points are 353×193 in the oscillatory

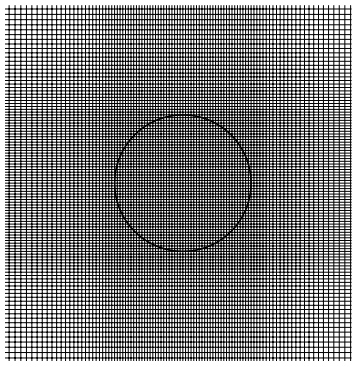

Fig. 7. Grid distribution near the cylinder for simulation of flow caused by its inline oscillation.

(x_r) and transverse (y_r) directions, respectively, and 30×30 grid points are uniformly distributed inside the cylinder (Fig. 7). The size of the computational domain used is $-50d < x_r < 50d$ and $-50d < y_r < 50d$, and the Neumann boundary conditions ($\partial u_i/\partial n_j = 0$) are used for all outer boundaries, where n_j is the vector normal to the outer boundary surface.

Fig. 8 shows the time history of the drag coefficient in the oscillatory direction, together with the numerical result of Dütsch et al. [17]. It is clear that the drag obtained from the present study agrees very well with that of Dütsch et al. [17]. Fig. 9 shows the profiles of the velocity component (u_a) along the y_a-axis at $x_a = -0.6d$ for three different phase positions, together with the experimental and numerical results of Dütsch et al. [17], where x_a and y_a are the oscillatory and transverse directions in the inertial reference frame, respectively. Again, the velocity profiles agree very well with the numerical and experimental results of Dütsch et al. [17]. The contours of the vorticity in the inertial reference frame for four different phase positions are shown in Fig. 10, where the vortex formation is characterized by two counter-rotating vortices

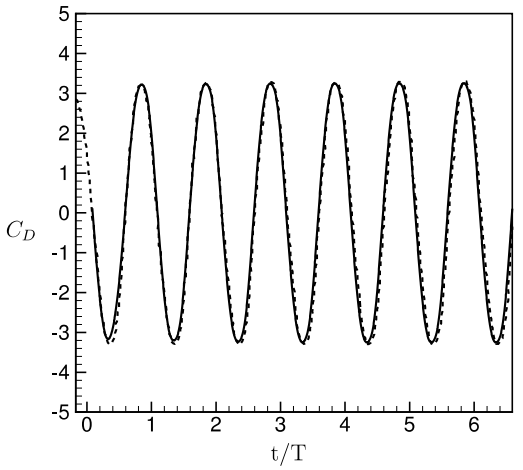

Fig. 8. Time history of the drag coefficient at $Re = 100$ and $KC = 5$: —, present study; – – –, Dütsch et al. [17].

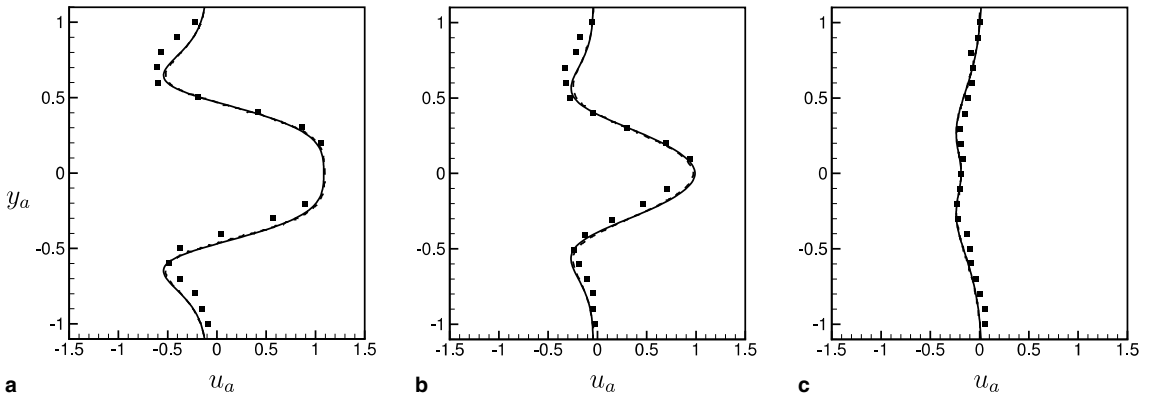

Fig. 9. Profiles of the velocity component (u_a) in the oscillatory direction (in the inertial reference frame) along the y_a-axis at $x_a = -0.6d$ for three different phase positions ($\phi = 2\pi ft$): (a) $\phi = 180°$; (b) $\phi = 210°$ and (c) $\phi = 330°$. —, Present study; – – –, numerical result of Dütsch et al. [17]; ■, experimental result of Dütsch et al. [17].

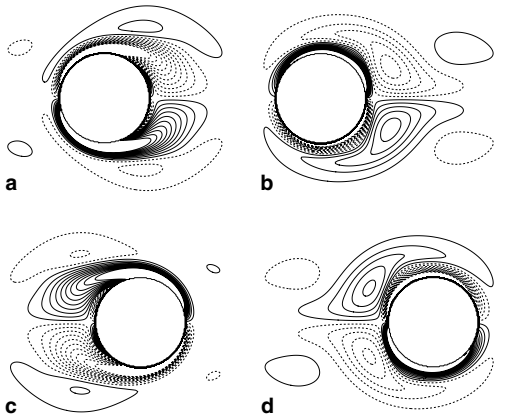

Fig. 10. Time sequence of the spanwise vorticity in the inertial reference frame: (a) $\phi = 0°$; (b) 96°; (c) 192° and (d) 288°. The contour levels are $\omega_z d/U_m = -8.5$ to 8.5 by increments of 0.85.

during the oscillation of the cylinder. This vortical structure is the same as that shown in Dütsch et al. [17], indicating that the present method accurately describes the vorticity field.

3.2. Transverse oscillation of a circular cylinder in a free-stream

In this section, we simulate the flow induced by a transverse oscillation of a circular cylinder in a free-stream. The Reynolds number is based on the free-stream velocity u_∞ and the cylinder diameter d. The transverse motion of the cylinder is given by a harmonic oscillation:

$$y_c(t) = A_m \cos(2\pi f_e t), \tag{35}$$

where y_c is the location of the cylinder center, A_m is the amplitude of the oscillation, and f_e is the oscillation frequency. The computation is performed at $Re = 185$, $A_m/d = 0.2$ and $0.8 \leqslant f_e/f_o \leqslant 1.2$ as in Guilmineau and Queutey [18], where f_o is the natural shedding frequency for a stationary cylinder. The numbers of grid points are 353×193 in the streamwise (x_r) and transverse (y_r) directions, respectively, and 30×30 grid

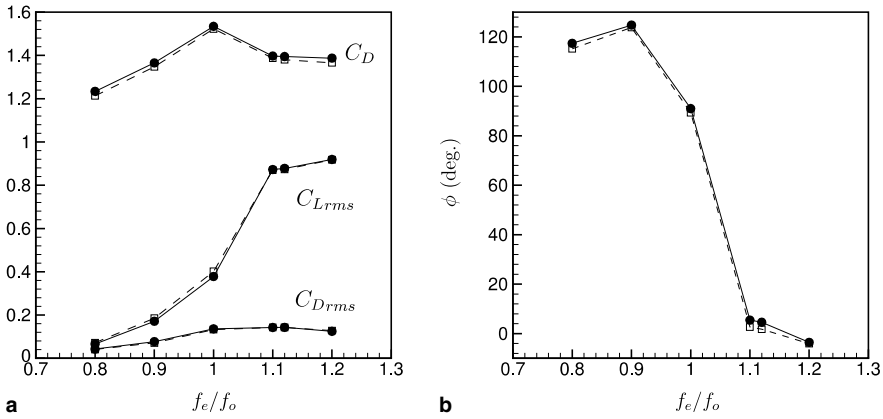

Fig. 11. Variations of the force coefficients and phase angle with respect to f_e/f_o (in the inertial reference frame): (a) mean drag coefficient (C_D) and rms drag and lift fluctuation coefficients (C_{Drms} and C_{Lrms}, respectively); (b) phase angle between C_L and the vertical position of the cylinder. –●–, Present study; –□–, Guilmineau and Queutey [18].

points are uniformly distributed inside the cylinder. The grid distribution is similar to that shown in Fig. 7. The size of the computational domain used is $-50d < x_r < 50d$ and $-50d < y_r < 50d$. A Dirichlet boundary condition ($u/u_\infty = 1$, $v = 0$) is used at the inflow, Neumann boundary conditions ($\partial u_i/\partial y_r = 0$) are used at farfield boundaries, and the convective boundary condition ($\partial u_i/\partial t + c\partial u_i/\partial x_r = 0$) is used at the outflow boundary, where c is the space-averaged streamwise velocity there.

Fig. 11(a) shows the variations of the mean drag and rms drag and lift fluctuation coefficients with respect to f_e/f_o. The phase angle between the lift coefficient and the vertical position of the cylinder is shown in Fig. 11(b). As shown, the present results agree very well with those of Guilmineau and Queutey [18]. Fig. 12 shows the vorticity contours when the oscillating cylinder locates at the extreme upper position. The vorticity pattern around the cylinder changes significantly between $f_e/f_o = 1.0$ and 1.1, which is the same as that observed by Guilmineau and Queutey [18].

4. Numerical examples of fluid–structure interaction problems

Two different unsteady flow problems are solved to show that the present method accurately describes the interaction between the fluid and the structure. A Cartesian coordinate system in a non-inertial reference frame is applied to both test problems.

4.1. Vortex-induced vibration of a circular cylinder

Flow-induced vibrations caused by vortex shedding from a structure is one of the representative fluid–structure interaction problems. Thus, we examine the vortex-induced vibration on an elastically mounted circular cylinder as a test problem of fluid–structure interaction. The motion of a circular cylinder is constrained only to a translational motion in x and y directions (i.e., no rotational motion is allowed), as was done in [19]. The Reynolds number is fixed at $Re = 200$ based on the free-stream velocity u_∞ and the cylinder diameter d. The non-dimensionalized governing equations for the motion of an elastically mounted cylinder in the inertial reference frame are

$$\ddot{x}_a + 4\xi\pi St\frac{f_n}{f_o}\dot{x}_a + \left(2\pi St\frac{f_n}{f_o}\right)^2 x_a = \frac{F_x}{n}, \tag{36}$$

$$\ddot{y}_a + 4\xi\pi St\frac{f_n}{f_o}\dot{y}_a + \left(2\pi St\frac{f_n}{f_o}\right)^2 y_a = \frac{F_y}{n}, \tag{37}$$

where ξ is the damping factor, f_o is the vortex shedding frequency of a fixed cylinder ($St = f_o d/u_\infty$), f_n is the natural frequency of the spring-damper-mass system, n is the mass ratio of solid to fluid, and F_x and F_y are the non-dimensional forces exerted on the cylinder in x and y directions, respectively. Here, $\boldsymbol{F}_N = (F_x, F_y)$ is obtained from Eq. (26) together with Eqs. (29) and (24). Then, Eqs. (36) and (37) are solved using the trapezoidal method after converting them into a system of first-order ordinary differential equations.

The values of mass ratio n and damping factor ξ are 10 and 0.01, respectively, as in Blackburn and Henderson [19]. In order to examine the lock-in region and associated phenomena, computations are performed at the range of $0.75 \leqslant f_n/f_o \leqslant 1.35$.

The numbers of grid points are 321×193 in the streamwise (x_r) and transverse (y_r) directions, respectively, and 30×30 grid points are uniformly distributed inside the cylinder. The size of the computational domain is $-20d < x_r < 50d$ and $-50d < y_r < 50d$. A Dirichlet boundary condition ($u/u_\infty = 1$, $v = 0$) is used at the inflow, Neumann boundary conditions ($\partial u_i/\partial y_r = 0$) are used at farfield boundaries, and the convective boundary condition ($\partial\ u_i/\partial t + c\partial u_i/\partial x_r = 0$) is used at the outflow boundary, where c is the space-averaged streamwise velocity there.

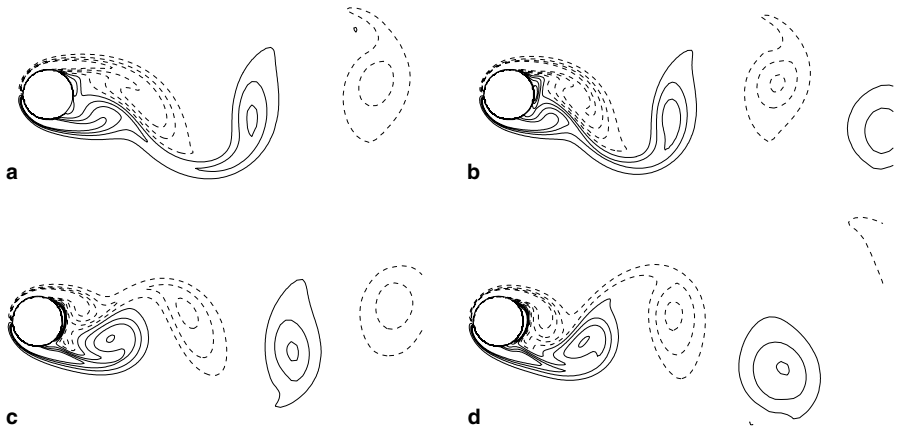

Fig. 12. Vorticity contours at the extreme upper position of the oscillating cylinder (in the inertial reference frame): (a) $f_e/f_o = 0.9$; (b) 1.0; (c) 1.1; (d) 1.2. The contour levels are $\omega_z d/u_\infty = -8$ to 8 by increments of 1.

Fig. 13 shows the variations of oscillation frequency (f_n'), mean drag and rms lift fluctuation coefficients (C_D and C_{Lrms}), and rms transverse displacement (y_{rms}) of the cylinder with respect to f_n/f_o. As shown in Fig. 13, the oscillation frequency f_n' is equal to f_n near $f_n = f_o$. This phenomenon is called lock-in, and the a amplitude of the transverse displacement increases considerably during lock-in. Outside this lock-in range, f_n' is almost same as f_o. The lock-in range, oscillation amplitude, drag and lift coefficients are nearly the same as those of Blackburn and Henderson [19].

Fig. 14 shows the vorticity contours when the cylinder is at the extreme upper position. In the non-lock-in region ($f_n/f_o = 0.75$ and 1.35), the vortex pattern around the cylinder is similar to that of the fixed cylinder, whereas it is very different in the lock-in region ($f_n/f_o = 1.0$).

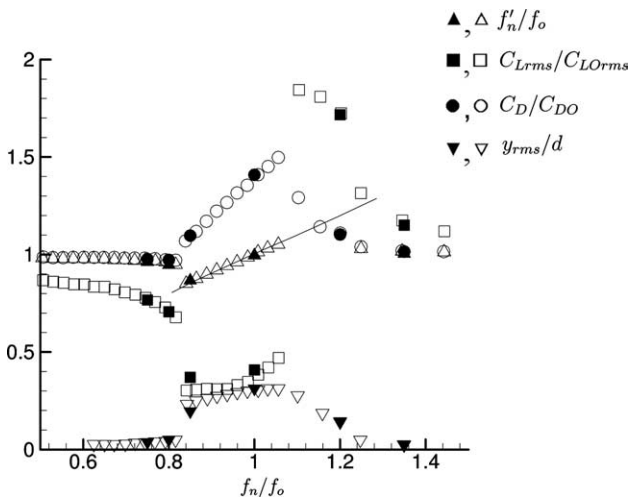

Fig. 13. Cylinder response diagram: f_n', oscillation frequency of the cylinder; C_{Lrms}, rms lift fluctuation coefficient; C_{LOrms}, rms lift fluctuation coefficient for the fixed cylinder; C_D, mean drag coefficient; C_{DO}, mean drag coefficient for the fixed cylinder; y_{rms}, rms transverse displacement of the cylinder. ▲, ■, ●, ▼, Present study; △, □, ○, ▽, Blackburn and Henderson [19]. The line in this figure corresponds to $f_n' = f_n$.

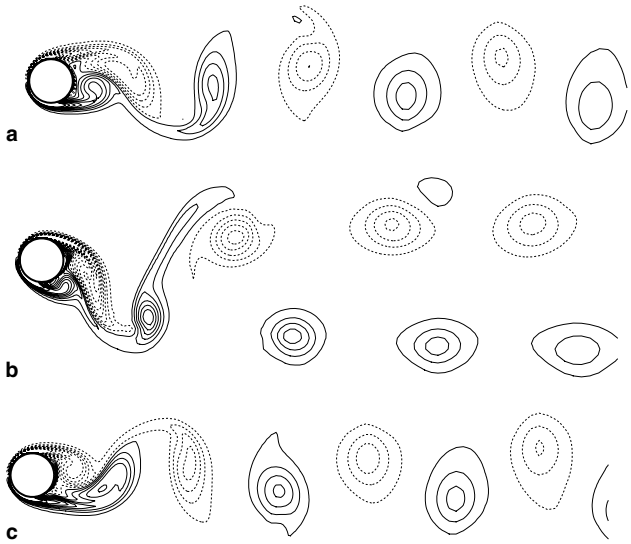

Fig. 14. Vorticity contours at the extreme upper position of the elastically mounted cylinder (in the inertial reference frame): (a) $f_n/f_o = 0.75$; (b) 1.0 and (c) 1.35.

4.2. Freely falling object under gravity

As the last flow problems, we consider freely falling sphere and cube under gravity, respectively. Unlike the vortex-induced vibration of a circular cylinder considered in the previous section, the object is not elastically mounted but it falls owing to the gravity. Thus, the motion of the body is governed by the Newton equation. The acceleration of the body by the gravity is $(\rho_s/\rho_f - 1)g$, where g is the gravitational acceleration, ρ_s and ρ_f are the densities of the sphere (or cube) and fluid, respectively. The Reynolds number is defined as

$$Re_g = \frac{(|(\rho_s/\rho_f) - 1|g)^{1/2} d^{3/2}}{\nu}, \tag{38}$$

where $u_c = (|(\rho_s/\rho_f) - 1|gd)^{1/2}$ is the characteristic velocity and d is the diameter of the sphere or the height of the cube.

For the present problem (see Eqs. (20) and (21)), $\mathbb{M} = \pi\rho_s\mathbb{I}/(6\rho_f)$, $\mathbb{I}_m = \pi\rho_s\mathbb{I}/(60\rho_f)$ for the sphere and $\mathbb{M} = \rho_s\mathbb{I}/\rho_f$, $\mathbb{I}_m = \rho_s\mathbb{I}/(6\rho_f)$ for the cube, and $\boldsymbol{T}_e = \boldsymbol{0}$. Thus, Eqs. (20) and (21) in the non-inertial reference frame become

$$\frac{d\boldsymbol{u}_s}{dt} + \boldsymbol{\Omega} \times \boldsymbol{u}_s = \mathbb{M}^{-1}\left[\boldsymbol{F}_N + \mathbb{M}\mathbb{R}^T \operatorname{sgn}\left(\frac{\rho_s}{\rho_f} - 1\right)\frac{\boldsymbol{g}}{|\boldsymbol{g}|}\right], \tag{39}$$

$$\frac{d\boldsymbol{\Omega}}{dt} = \mathbb{I}_m^{-1}\boldsymbol{T}_N. \tag{40}$$

Here, $\boldsymbol{u}_s$ and $\boldsymbol{\Omega}$ are the translational and rotational velocities of the body in the non-inertial reference frame, respectively, and determined by solving Eq. (28). $\boldsymbol{F}_N$ and $\boldsymbol{T}_N$ are the non-dimensional force and moment exerted on the body by fluid in the non-inertial reference frame, respectively.

For the case of sphere, we consider two different cases as considered in Mordant and Pinton [20]: the first is $\rho_s/\rho_f = 2.57$ and $Re_g = 48.5$, and the second is $\rho_s/\rho_f = 7.86$ and $Re_g = 287$. The computational domain is $-30d \leqslant x_r \leqslant 30d$, $-30d \leqslant y_r \leqslant 30d$ and $-30d \leqslant z_r \leqslant 30d$. The numbers of grid points are

$129(x_r) \times 129(y_r) \times 129(z_r)$, and $30 \times 30 \times 30$ grid points are uniformly distributed inside the sphere. Neumann boundary conditions ($\partial u_i/\partial n_j = 0$) are used for all outer boundaries, where n_j is the vector normal to the outer boundary surface. On the other hand, for the case of cube, we consider the case of $\rho_s/\rho_f = 7.86$ and $Re_g = 208$ such that the cube has the same volume of the sphere at $Re_g = 287$. Other computational parameters are the same as those for the sphere case.

Fig. 15 shows the temporal evolution of the velocity of the sphere in the gravitational direction at $Re_g = 48.5$ and 287, together with the experimental results of Mordant and Pinton [20]. For $Re_g = 48.5$,

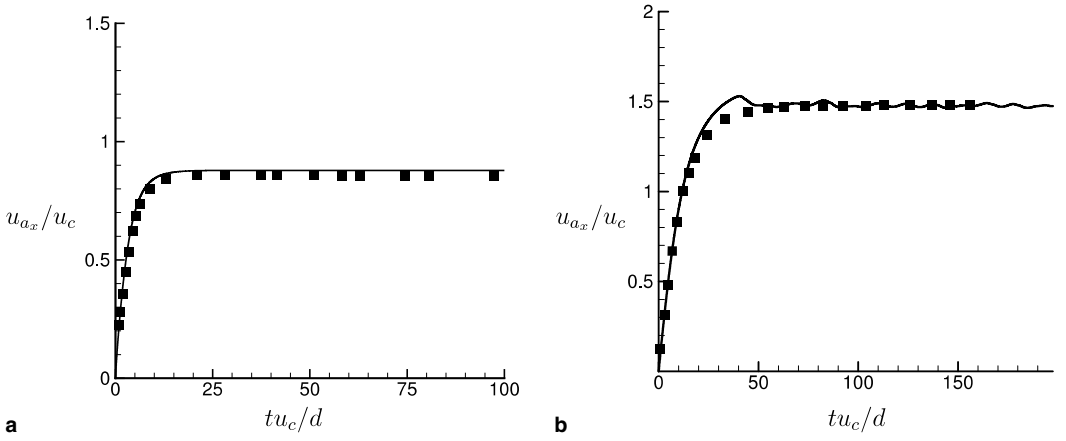

Fig. 15. Temporal evolution of the velocity of the sphere in the gravitational direction (in the inertial reference frame): (a) $Re_g = 48.5$; (b) $Re_g = 287$. —, Present study; ■, Mordant et al. [20].

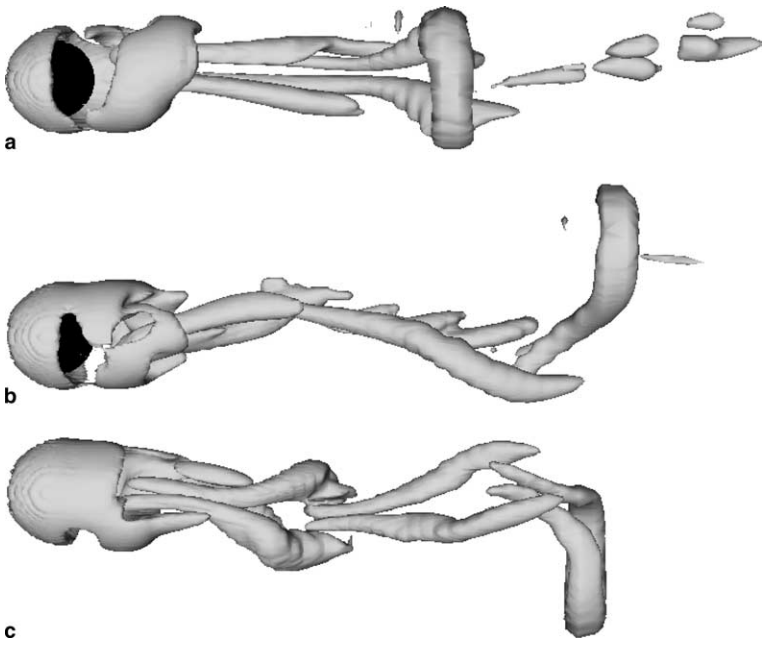

Fig. 16. Instantaneous vortical structures at $Re_g = 287$: (a) $tu_c/d = 335.4$; (b) 352.5 and (c) 366.2.

the sphere accelerates monotonically and reaches a terminal velocity in a finite time as shown in Fig. 15(a). Other velocity components and rotation of the sphere remain zero. The Reynolds number based on this terminal velocity and the sphere diameter is about 42, at which flow over a stationary sphere is steady axi-symmetric. For $Re_g = 287$, however, the velocity of the sphere oscillates after reaching its maximum value. On the other hand, this oscillation was not observed by Mordant and Pinton [20], possibly because the sphere motion was ensemble averaged from 10 experiments and it was not possible to measure these small oscillations experimentally as reported in Mordand and Pinton [20]. The Reynolds number based on the terminal velocity for $Re_g = 287$ is about 430, at which the fixed sphere shows unsteady asymmetric flow [21,22]. That is, vortex shedding behind the sphere loses the planar and axi-symmetry and the shedding

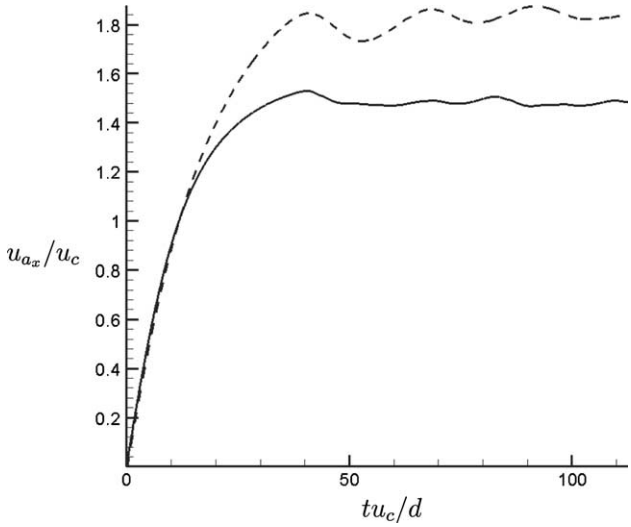

Fig. 17. Temporal evolutions of the velocity in the gravitational direction for the cases of sphere and cube: —, sphere ($Re_g = 287$); – – –, cube ($Re_g = 208$).

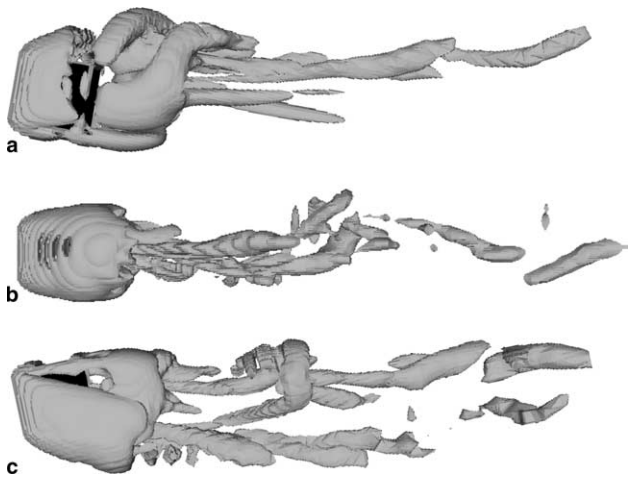

Fig. 18. Instantaneous vortical structures at $Re_g = 208$: (a) $tu_c/d = 114.0$; (b) 125.1 and (c) 148.2.

direction changes irregularly. Fig. 16 shows the vortical structures at three different instants for $Re_g = 287$ using the vortex-identification method of Jeong and Hussain [23]. It is clear that the direction of vortex loops changes in time.

Fig. 17 shows the temporal evolutions of the velocity in the cases of cube and sphere, respectively, at $Re_g = 208$ and $Re_g = 287$. The terminal velocity of cube is higher than that of sphere because the cross-sectional area of cube is smaller than that of sphere when both volumes are set to be equal. For the grid-independent solution, we doubled the grids but obtained the same results. Fig. 18 shows the vortical structures at three different instants for $Re_g = 208$ using the vortex-identification method of Jeong and Hussain [23]. The direction of vortex loops changes in time because of the rotation of cube (the rotation of cube is manifest in Fig. 18).

5. Conclusions

In the present study, we developed an immersed boundary method in a non-inertial reference frame in order to simulate flow around an arbitrarily moving body in an infinite domain, including forced motion and fluid–structure interaction problems. The present method is based on the previous immersed boundary method by Kim et al. [12] designed for flow over a stationary body. The governing equations in the non-inertial reference frame are formulated in a strongly conservative form that provides a good numerical stability (see also [6]). For the fluid–structure interaction problems, fully coupled Navier–Stokes and dynamic equations are solved without any iteration per time step.

In the case of forced motion, inline and cross-flow oscillations of a circular cylinder, respectively, were simulated using the present numerical method. For fluid–structure interaction problems, vortex-induced vibration of a circular cylinder, and freely falling sphere and cube under gravity were examined. All the flow problems considered produced excellent agreements with the previous numerical and experimental results, indicating the applicability and accuracy of the present immersed boundary method for flow around an arbitrarily moving body.

Acknowledgment

This work was supported by the Creative Research Initiatives Program of the Korean Ministry of Science and Technology.

References

[1] T.E. Tezduyar, M. Behr, J. Liou, A new strategy for finite element computations involving moving boundaries and interfaces – The deforming-spatial-domain/space-time procedure: I. The concept and the preliminary numerical tests, Computer Methods in Applied Mechanics and Engineering 94 (1992) 353.
[2] W. Noh, P. Woodward, A simple line interface calculation, in: Proceedings of the Fifth International Conference on Numerical Methods in Fluid Dynamics, Springer, 1976.
[3] S. Osher, J.A. Sethian, Fronts propagating with curvature-dependent speed: algorithms based on Hamilton–Jacobi formulations, Journal of Computational Physics 79 (1988) 12.
[4] A.E. Gill, Atmosphere-Ocean Dynamics, International Geographics Series, vol. 30, Academic Press, 1982.
[5] W. Kley, On the treatment of the Coriolis force in computational astrophysics, Astronomy and Astrophysics 338 (1998) L37.
[6] M. Beddhu, L.K. Taylor, D.L. Whitfield, Strong conservative form of the incompressible Navier–Stokes equations in a rotating frame with a solution procedure, Journal of Computational Physics 128 (1996) 427.
[7] K.C. Hall, Eigenanalysis of unsteady flows about airfoils, cascades, and wings, AIAA Journal 32 (1994) 2426.
[8] I. Robertson, L. Li, S.J. Sherwin, P.W. Bearman, A numerical study of rotational and transverse galloping rectangular bodies, Journal of Fluids and Structures 17 (2003) 681.

[9] H.H. Hu, D.D. Joseph, M.J. Crochet, Direct numerical simulation of fluid particle motions, Theoretical and Computational Fluid Dynamics 3 (1992) 285.
[10] I. Jadic, R.M.C. So, M.P. Mignolet, Analysis of fluid–structure interactions using a time marching technique, Journal of Fluids and Structures 12 (1998) 631.
[11] C.Y. Zhou, R.M.C. So, K. Lam, Vortex-induced vibrations of an elastic circular cylinder, Journal of Fluids and Structures 13 (1999) 165.
[12] J. Kim, D. Kim, H. Choi, An immersed-boundary finite-volume method for simulations of flow in complex geometries, Journal of Computational Physics 171 (2001) 132.
[13] G. Yun, H. Choi, D. Kim, Turbulent flow past a sphere at $Re = 3700$ and 10,000, Physics of Fluids 15 (2003) S6.
[14] J.M. McCarthy, An Introduction to Theoretical Kinematics, The MIT Press, 1990.
[15] P. Moin, Fundamentals of Engineering Numerical Analysis, Cambridge University Press, 2001.
[16] W.L. Briggs, V.E. Henson, S.F. Mccormick, A Multigrid Tutorial, Siam, 2000.
[17] H. Dütsch, F. Durst, S. Becker, H. Lienhart, Low-Reynolds-number flow around an oscillating circular cylinder at low Keulegan–Carpenter numbers, Journal of Fluid Mechanics 360 (1998) 249.
[18] E. Guilmineau, P. Queutey, A numerical simulation of vortex shedding from an oscillating circular cylinder, Journal of Fluids and Structures 16 (6) (2002) 773.
[19] H. Blackburn, R. Henderson, Lock-in behavior in simulated vortex-induced vibration, Experimental Thermal and Fluid Science 12 (1996) 184.
[20] N. Mordant, J.-F. Pinton, Velocity measurement of a settling sphere, The European Physical Journal B 18 (2000) 343.
[21] H. Sakamoto, H. Haniu, A study on vortex shedding from spheres in a uniform flow, Transaction of ASME: Journal of Fluids Engineering 112 (1990) 386.
[22] R. Mittal, Planar symmetry in the unsteady wake of a sphere, AIAA Journal 37 (1999) 388.
[23] J. Jeong, F. Hussain, On the identification of a vortex, Journal of Fluid Mechanics 285 (1995) 69.